# Production of neutron-rich actinide isotopes in isobaric collisions via multinucleon transfer reactions*

Peng-Hui Chen,[1,†] Chang Geng,[1] Zu-Xing Yang,[2] Xiang-Hua Zeng,[1,3] and Zhao-Qing Feng[4]

[1]*School of Physical Science and Technology, Yangzhou University, Yangzhou 225009, China*
[2]*RIKEN Nishina Center, Wako, Saitama 351-0198, Japan*
[3]*College of Electrical, Power and Energy Engineering, Yangzhou University, Yangzhou 225009, China*
[4]*School of Physics and Optoelectronics, South China University of Technology, Guangzhou 510641, China*

We have calculated the multinucleon transfer reactions of $^{208}$Os, $^{208}$Pt, $^{208}$Hg, $^{208}$Pb,$^{208}$Po, $^{208}$Rn, $^{208}$Ra,$^{132,136}$Xe bombarding on $^{232}$Th and $^{248}$Cm at Coulomb barrier energies within the dinuclear system model, systematically. The results are in good agreement with the available experimental data. The Coulomb effect and shell effect on the production of actinides in these reactions have been investigated thoroughly. Potential energy surface and total kinetic energy mass distributions in the reactions $^{208}$Hg, $^{208}$Pb and$^{208}$Po colliding on $^{248}$Cm and $^{232}$Th are calculated and analyzed, respectively. It is found that PES and TKE spectra manifest the fragment formation mechanism in the multinucleon transfer reactions. The isospin effect and shell effect are shown in PES and TKE. Production cross-sections of multinucleon transfer products are highly dependent on the isobar projectiles with the mass number $A = 208$. The isobar projectiles with larger N/Z ratios are favorable for creating neutron-rich target-like fragments. The isobar projectiles with larger charge number induced products tend to shift to proton-rich regions. Coulomb potential coupled with the shell effect is shown in production cross-sections of actinide isotopes. Based on the radioactive projectiles induced reactions, we have predicted massive new actinide isotopes around nuclear drip lines, even could access the superheavy nuclei region.

Keywords: Dinuclear system model, Isobaric collisions, Multinucleon transfer reactions, Neutron-rich actinides



## I. INTRODUCTION

So far, including the synthesis of eleven isotopes $^{149}$Lu [1], $^{207}$Th[2],$^{251,264}$Lr[3, 4], $^{166}$Pm, $^{168}$Sm, $^{170}$Eu, $^{172}$Gd[5], $^{204}$Ac[6], $^{39}$Na[7] and $^{286}$Mc[8] in the last year, there are 3327 species nuclei existed in the nuclide chart as known, which consist of 288 natural nuclides (254 stable isotopes longer-lived than the earth and 34 unstable nuclides) and 3039 species nuclei synthesized in laboratories over the world based on methods of fusion-evaporation (FE), multinucleon transfer (MNT) or deep inelastic reactions (DIR), projectile fragmentation (PF), spallation, fission (SF), neutron capture (NC), thermonuclear test (TT)[9]. However, there may be 8000-10000 unknown bounded isotopes predicted to exist by some theoretical models[10–12] in the nuclei chart. Therefore, at least, over 5000 nuclides are waiting to be found in laboratories by nuclear experimentalists, especially in the regions of nuclear drip lines and stability island of superheavy nuclei.

In recent years, from the experiment side, laboratories all over the world have synthesized several new species nuclei such as $^{207}$Th, $^{235}$Cm, $^{214}$U, $^{222}$Np, $^{211}$Pa, $^{280}$Ds[2, 13–15] *etc.* produced by FE reactions, $^{110}$Zr, $^{121}$Tc and $^{129}$Pd *etc.* produced by PF[16], $^{223,229}$Am and $^{233}$Bk [17] *etc.* produced by MNT. It draws lots of interest, for Lanzhou Heavy Ion Research Facility (HIRFL) in China, Joint Institute for Nuclear Research (JINR) in Russia, Helmholtz Centre for Heavy Ion Research (GSI) in Germany and Grand Accëlërateur National d'Ions Lourds (GANIL) in France and Argonne national laboratory (ANL) in America, to synthesize new nuclides around drip lines and superheavy region.

In order to describe the damped collision mechanism and predict synthesis cross-sections of the objective nuclides, theorists have built some sophisticated and practical models to depict the multinucleon transfer reactions at incident energy near the Coulomb barrier. For example, the GRAZING model[18–20], the dinuclear system (DNS) model[21–30], and a dynamical model based on the Langevin equations[31, 32]. Microscopic methods based on the degree of freedom of nucleons include the Time-dependent Hartree-Fock (TDHF) approach[33–35], and the improved quantum molecular dynamics model (ImQMD)[36, 37]. Generally, all of these models could nicely reproduce the available experimental data through their unique characteristics. The dinuclear system model (DNS) can better consider the shell effect, dynamical deformation, fission, quasi-fission, deep-inelastic mechanisms, and odd-even effect, and its calculation efficiency is very high.

In this work, the calculated cross sections of target-like fragments in MNT reactions of $^{132,136}$Xe + $^{248}$Cm at incident energy around Coulomb barriers have been compared to the available experimental data based on the DNS model. To investigate the Coulomb force coupled with the shell effect in the MNT process, isobaric projectiles with mass number A = 208 around the doubly magic nucleus $^{208}$Pb are selected to bombard targets $^{232}$Th and $^{248}$Cm at Coulomb barrier energies. We analyzed production cross-sections of unknown actinide isotopes in the isobaric collisions. The article is or-

* Supported by National Natural Science Foundation of China (No. 12105241, 12175072), Natural Science Foundation of Jiangsu Province (No. BK20210788), Jiangsu Provincial Double-Innovation Doctoral Program (No. JSSCBS20211013), University Science Research Project of Jiangsu Province (No. 21KJB140026), Lv Yang Jin Feng (No. YZLYJFJH2021YXBS130), and Key Laboratory of High Precision Nuclear Spectroscopy, Institute of Modern Physics, Chinese Academy of Sciences (No. IMPKFKT2021001)

† Corresponding author,chenpenghui@yzu.edu.cn

ganized as follows: In Sec. II we give a brief description of the DNS model. Calculated results and discussions are presented in Sec. III. A summary is concluded in Sec. IV.

## II. MODEL DESCRIPTION

Initially, the DNS concept was proposed by Volkov for depicting deep inelastic heavy-ion collisions[38]. G.G. Adamian added quasifission component in massive fusion process[39, 40]. Finally, the modifications of the relative motion energy and angular momentum of two colliding nuclei coupling to nucleon transfer within the DNS concept were developed by the Lanzhou Group [41]. The production cross-sections of SHN, quasi-fission, and fusion-fission dynamics have been extensively investigated within the dynamical DNS model. The dynamical evolution of colliding system sequentially proceeds the capture process by overcoming the Coulomb barrier to form the DNS, relaxation process of the relative motion energy, angular momentum, mass, charge asymmetry, *etc.* within the potential energy surface and the de-excitation of primary fragments[42]. The production cross-section of the MNT fragments was evaluated by

$$\sigma_{\rm tr}(Z_1,N_1,E_{c.m.}) = \sum_{J=0}^{J_{\rm max}} \sigma_{cap}(E_{\rm c.m.},J)\int f(B)$$
$$\times P(Z_1,N_1,J_1,B)\times W_{\rm sur}(E_1,J_1,s)dB. \quad (1)$$

The $\sigma_{\rm cap}(E_{\rm c.m.},J)$ is the cross-sections of DNS formation derived by the Hill-Wheeler formula with barrier distribution function[43]. $W_{\rm sur}(E_1,J_1,s)$ is the survival probability of fragments formation in the MNT process. The s stands for the decay channels for fragments $(Z_1,N_1)$, such as neutron, proton, deuteron, alpha, gamma rays, etc. $E_{\rm c.m.}$ is incident energy in the center of the mass frame. The largest angular momentum $J_{\rm max}$ was calculated at the grazing configuration for the colliding system. The angular momentum $J$ is taken at the initial colliding configuration before dissipating. $E_1$ and $J_1$ represent the excitation energy and angular momentum for the fragment with proton number $Z_1$ and neutron number $N_1$ in dinuclear system model (DNS), respectively. $P(Z_1,N_1,J_1,B)$ is formation probability of fragments $(Z_1,N_1)$. For the barrier distribution function, we take the asymmetry Gaussian[44] form.

$$f(B) = \frac{1}{N}\exp[-(\frac{B-B_m}{\triangle})^2] \quad (2)$$

The quantities $\triangle$ and $B_{\rm m}$ were evaluated by $\triangle$ =($B_{\rm t}$+$B_{\rm s}$)/2, $B_{\rm m}$=($B_{\rm t}$+$B_{\rm s}$)/2. $B_{\rm t}$ and $B_{\rm s}$ represent the height of the Coulomb barrier and the minimum point of deformation under tip-tip collision respectively. The normalization constant satisfies $\int f(B)dB = 1$.

In the DNS model, the solution of nucleon transfer and relative motion carries out a set of microscopic derivations, master equations distinguish proton and neutron. The fragments distribution probability, P$(Z_1,N_1,E_1)$ represents the proton number $Z_1$, neutron number $N_1$, and excitation energy $E_1$ for DNS fragment 1 is described by the following master equation

$$\frac{dP(Z_1,N_1,E_1,\beta,t)}{dt} =$$
$$\sum_{Z_1'} W_{Z_1,N_1,\beta;Z_1',N_1,\beta'}(t)[d_{Z_1,N_1}P(Z_1',N_1,E_1',\beta^{'},t)$$
$$-d_{Z_1',N_1}P(Z_1,N_1,E_1,\beta,t)]$$
$$+\sum_{N_1'} W_{Z_1,N_1,\beta;Z_1,N_1',\beta'}(t)[d_{Z_1,N_1}P(Z_1,N_1',E_1',\beta^{'},t)$$
$$-d_{Z_1,N_1'}P(Z_1,N_1,E_1,\beta,t)]$$
$$-[\Lambda^{\rm qf}_{A_1,E_1,t}(\Theta)+\Lambda^{\rm fis}_{A_1,E_1,t}(\Theta)]P(Z_1,N_1,E_1,t) \quad (3)$$

The $W_{Z_1,N_1,\beta;Z_1',N_1,\beta}(W_{Z_1,N_1,\beta,;Z_1,N_1',\beta})$ is the mean transition probability from the channel$(Z_1,N_1,E_1,\beta)$ to $(Z_1^{'},N_1,E_1^{'},\beta)$, [or $(Z_1,N_1,E_1,\beta)$ to $(Z_1,N_1^{'},E_1^{'},\beta)$], and $d_{Z_1,Z_1}$ denotes the microscopic dimension corresponding to the macroscopic state $(Z_1,N_1,E_1)$. The sum is taken over all possible proton and neutron numbers that fragment ($Z_1^{'}$,$N_1^{'}$) may take, but only one nucleon transfer is considered in the model with the relations $Z_1^{'}=Z_1\pm1$ and $N_1^{'}=N_1\pm1$. The quasi-fission width $\Lambda^{\rm qf}$ and fission width $\Lambda^{\rm fis}$ are calculated by the Kramers formula [45, 46].

The excited DNS opens a valence space in which the valence nucleons have a symmetrical distribution around the Fermi surface. Only the particles at the states within the valence space are actively for nucleon transfer. The transition probability is related to the local excitation energy and nucleon transfer, which is microscopically derived from the interaction potential in valence space as described as [47, 48].

$$W_{Z_1,N_1,\beta;Z_1',N_1,\beta'} = \frac{\tau_{\rm mem}(Z_1,N_1,\beta,E_1;Z_1',N_1\beta',E_1')}{d_{Z_1,N_1}d_{Z_1',N_1}\hbar^2}\times$$
$$\sum_{ii'}|\langle Z_1',N_1,E_1',i'|V|Z_1,N_1,E_1,i\rangle|^2. \quad (4)$$

The neutron transition coefficient has the same formula. The relaxation time is calculated using the method of deflection function[49]. Memory time $\tau_{\rm mem}$ and $V$ interaction elements can be seen in the Ref[47].

The motion of nucleons in the interacting potential is governed by the single-particle Hamiltonian[41, 50] as

$$H(t) = H_0(t) + V(t) \quad (5)$$

with

$$H_0(t) = \sum_K\sum_{\nu_K}\varepsilon_{\nu_K}(t)\alpha^+_{\nu_K}(t)\alpha_{\nu_K}(t) \quad (6)$$
$$V(t) = \sum_{K,K'}\sum_{\alpha_K,\beta_{K'}}u_{\alpha_K,\beta_{K'}}\alpha^+_{\alpha_K}(t)\alpha_{\beta_K}(t) \quad (7)$$
$$= \sum_{K,K'}V_{K,K'}(t)$$

Here the indices $K$, $K'$ ($K,K'$ = 1, 2) denote the fragment 1 and 2. The quantities $\varepsilon_{\nu{\rm K}}$ and $u_{\alpha_{\rm K},\beta_{\rm K'}}$ represent the single-particle energies and the interaction matrix elements, respectively. The single-particle states are defined with respect to

the centers of the interacting nuclei and are assumed to be orthogonalized in the overlap region. So the annihilation and creation operators are dependent on time. The single-particle matrix elements are parameterized by

$$u_{\alpha_{\rm K},\beta'_{\rm K}} = \tag{8}$$
$$U_{\rm K,K'}(t)\left\{\exp\left[-\frac{1}{2}(\frac{\varepsilon_{\alpha_{\rm K}}(t)-\varepsilon_{\beta_{\rm K}}(t)}{\Delta_{\rm K,K'}(t)})^2\right]-\delta_{\alpha_{\rm K},\beta_{\rm K'}}\right\}$$

The detailed calculation of these parameters and the mean transition probabilities were described in Ref. [41, 50].

$$\Delta\varepsilon_{\rm K}=\sqrt{\frac{4\varepsilon^*_{\rm K}}{g_{\rm K}}},\quad \varepsilon^*_{\rm K}=\varepsilon^*\frac{A_{\rm K}}{A},\quad g_{\rm K}=A_{\rm K}/12, \tag{9}$$

Where the $\varepsilon^*$ is the local excitation energy of the DNS. The microscopic dimension for the fragment $(Z_K, N_K)$ is evaluated by the valence states $N_K = g_K\Delta\varepsilon_K$ and the valence nucleons $m_K = N_K/2$ $(K = 1, 2)$ as

$$d(m_1,m_2)=\binom{N_1}{m_1}\binom{N_2}{m_2}. \tag{10}$$

The local excitation energy $E_1$ was derived by the dissipation energy coulpled to potential energy surface (PES) of the relative motion of DNS. The excitation energy in the equilibrium stage is owned by the fragments divided by mass. The angular momentum of the main fragment is determined by the moment of inertia. The local excitation energy evaluated by[47, 48]

$$\varepsilon^*(t)=E^{\rm diss}(t)-\left(U(\{\alpha\})-U(\{\alpha_{\rm EN}\})\right). \tag{11}$$

The entrance channel quantities $\{\alpha_{\rm EN}\}$ include the proton and neutron numbers, quadrupole deformation parameters and orientation angles being $Z_{\rm P}, N_{\rm P}, Z_{\rm T}, N_{\rm T}, R, \beta_{\rm P}, \beta_{\rm T}, \theta_{\rm P}, \theta_{\rm T}$ for projectile and target nuclei with the symbols of $P$ and $T$, respectively. The interaction time $\tau_{\rm int}$ is obtained from the deflection function method [51]. The energy dissipated into the DNS increase exponentially. The potential energy surface (PES) of the DNS is evaluated by

$$\begin{aligned}U_{\rm dr}(t)&=Q_{\rm gg}+V_{\rm C}(Z_1,N_1;\beta_1,Z_2,N_2,\beta_2,t)\\&+V_{\rm N}(Z_1,N_1,\beta_1;Z_2,N_2,\beta_2,t)+V_{\rm def}(t)\end{aligned} \tag{12}$$

with

$$V_{\rm def}(t)=\frac{1}{2}C_1(\beta_1-\beta'_T(t))^2+\frac{1}{2}C_2(\beta_2-\beta'_P(t))^2 \tag{13}$$

$$C_i=(\lambda-1)(\lambda+2)R_{\rm N}^2\delta-\frac{3}{2\pi}\frac{Z^2e^2}{R_{\rm N}(2\lambda+1)}. \tag{14}$$

Where, the $Q_{\rm gg}$ derived by the negative binding energies of the fragments $(Z_{\rm i}, N_{\rm i})$ were calculated by liquid drop model plus shell correction[11]. The $\theta_i$ denotes the angles between the collision orientations and the symmetry axes of the deformed nuclei. $V_{\rm C}$ and $V_{\rm N}$ were calculated by the Wong formular[52] and double-folding potential[53], respectively. The quadrupole deformations of the ground state nuclei are taken from Ref. [54]. $V_{\rm def}(t)$ is the deformation energy of DNS at the reaction time $t$. The evolutions of quadrupole deformations of projectile-like and target-like fragments undergo from the initial configuration as

$$\begin{aligned}\beta'_{\rm T}(t)&=\beta_{\rm T}\exp(-t/\tau_\beta)+\beta_1[1-\exp(-t/\tau_\beta)],\\ \beta'_{\rm P}(t)&=\beta_{\rm P}\exp\left(-t/\tau_\beta\right)+\beta_2[1-\exp(-t/\tau_\beta)]\end{aligned} \tag{15}$$

with the deformation relaxation is $\tau_\beta = 4\times10^{-21}$ $s$.

The total kinetic energy (TKE-mass) of the primary fragment is evaluated by the following expression.

$$\mathrm{TKE}=\mathrm{E_{c.m.}}+\mathrm{Q_{gg}}-\mathrm{E^{diss}}, \tag{16}$$

where $Q_{\rm gg} = M_{\rm P} + M_{\rm T} - M_{\rm PLF} - M_{\rm TLF}$ and $E_{\rm c.m.}$ is the incident energy in the center of mass frame. The mass $M_{\rm P}$, $M_{\rm T}$, $M_{\rm PLF}$ and $M_{\rm TLF}$ correspond to the projectile, target, projectile-like fragment, and target-like fragment, respectively.

The survival probability $W_{\rm sur}(E_1, J_1, s)$ is particularly important in the evaluation of the cross-section, which is usually calculated with the statistical model. The physical process of understanding the excited nucleus is clear. However, the magnitude of survival probability was strongly dependent on the ingredients in the statistical model, such as level density parameter[55], separation energy [54], shell correction[54], fission barrier[56, 57], *etc.*. The excited fragments were cooled by evaporating $\gamma$-rays, light particles (neutrons, protons, $\alpha$, *etc.*) in competition with fission[44]. the probability in the channel of evaporating the $x-$th neutron, the $y-$th proton and the $z-$ alpha is expressed as

$$\begin{aligned}&W_{\rm sur}(E_1^*,x,y,z,J)=P(E_1^*,x,y,z,J)\\&\times\prod_{i=1}^{x}\frac{\Gamma_n(E_{\rm i}^*,J)}{\Gamma_{\rm tot}(E_{\rm i}^*,J)}\prod_{j=1}^{y}\frac{\Gamma_p(E_{\rm j}^*,J)}{\Gamma_{\rm tot}(E_{\rm j}^*,J)}\prod_{k=1}^{z}\frac{\Gamma_\alpha(E_{\rm k}^*,J)}{\Gamma_{\rm tot}(E_{\rm k}^*,J)}\end{aligned} \tag{17}$$

Here the $E_1^*$, $J$ are the excitation energy evaluated from the mass table in Ref. [11] and the spin of the excited nucleus, respectively. The total width $\Gamma_{\rm tot}$ is the sum of partial widths of particle evaporation, $\gamma$-emission, and fission. The excitation energy $E_s^*$ before evaporating the $s$-th particle is evaluated by

$$E_{s+1}^*=E_s^*-B_{\rm i}^n-B_{\rm j}^{\rm p}-B_{\rm k}^\alpha-2T_{\rm s} \tag{18}$$

with the initial condition $E_1^*$ and $\rm s = i + j + k$. The $B_i^n$, $B_j^p$, $B_k^\alpha$ are the separation energy of the $i$-th neutron, $j$-th proton, $k$-th alpha, respectively. The nuclear temperature $T_i$ is given by $E_{\rm i}^* = aT_{\rm i}^2 - T_{\rm i}$ with $a$ being the level density parameter. The fission width and particle decay width were calculated by the Weisskopf evaporation theory and the Bohr-Wheeler formula, respectively. The realization probability $P(E_1^*, x, y, z, J)$ was calculated by the Jackson formula[58].

## III. RESULTS AND DISCUSSION

We calculated the production cross-sections of actinide isotopes chains with the atomic number $Z = 93-100$ in collisions of $^{132,136}$Xe + $^{248}$Cm at incident energy $E_{\rm lab}$ = 699-790 MeV, as shown in Fig. 1. Comparing to the available experimental data of $^{129,132,136}$Xe + $^{248}$Cm which were

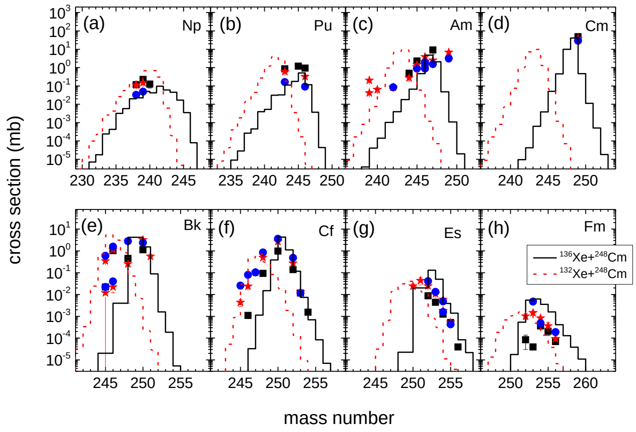


Fig. 1. (Color online) Calculation and experiment results of production cross-sections of actinide isotopic chains with Z = 93-100 in reactions of $^{129,132,136}$Xe + $^{248}$Cm at $E_{\rm lab}$ = 699-790 MeV. The available experimental data are taken from [59, 60], marked by solid black square for $^{136}$Xe induced reactions, solid red circle for $^{132}$Xe induced reactions, solid blue star for $^{129}$Xe induced reactions
. Our calculations for $^{136}$Xe induced reactions were shown by solid black lines, $^{132}$Xe induced reactions shown by dash red lines.

represented by a solid red star, solid blue circle, and solid black squares with error bars, respectively, our calculation of $^{136}$Xe + $^{248}$Cm marked by solid black lines and $^{132}$Xe + $^{248}$Cm marked by dash red lines could basically reproduce the tendency of cross-sections distribution of actinide isotopic chains. From experimental data[59, 60], it was found that projectiles $^{129,132,136}$Xe isotopes induced reactions with target $^{248}$Cm gave actinide products which have a large overlap distribution area in the neutron-rich region. It was not distinguishable clearly as we expected. From our calculation in terms of deep-inelastic mechanism, relative proton-rich projectiles $^{132}$Xe induced reactions tend to shift to the proton-rich region, compared to experimental results. According to the data in Fig. 1, target-like fragments have production cross-sections of magnitude levels from 100 millibarns to 10 nanobarns. Too far off the target, the formation cross section of target-below products decreases more slowly than trans-target products, which indicates quasi-fission was dominant in this collisions relatively. It should be noted that the limits of our calculation are in the free parameter model dependence in the calculation of primary fragments cross section and in the estimation of the survival probability to fission.

To investigate the competition of Coulomb repulsive potential and shell effect in MNT reactions, we calculated reactions of isobaric projectiles with $A = 208$ bombarding on targets $^{248}$Cm and $^{232}$Th at incident energy $E_{\rm c.m.} = 1.1 \times V_{\rm B}$. Calculations detail for these collisions would be shown below. Interaction potential between colliding partners was combined with Coulomb potential and nuclear potential. In Fig. 2 (a), interaction potential $V_{\rm CN}$ of $^{208}$Pt + $^{248}$Cm, $^{208}$Hg + $^{248}$Cm, $^{208}$Pb + $^{248}$Cm, $^{208}$Po + $^{248}$Cm and $^{208}$Rn + $^{248}$Cm reactions were marked by solid black, dash red, dash-dot blue, dash-dot-dot green, short dash olive lines, respectively. The

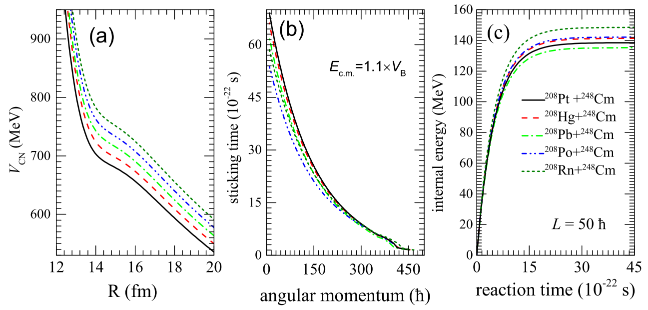


Fig. 2. (Color online) The solid black, red, blue, green, olive lines indicate the interaction potential of the tip-tip collisions as a function of surface distance for reactions of projectiles $^{208}$Hg, $^{208}$Pb, $^{208}$Po, $^{208}$Pt and $^{208}$Rn induced reactions with target $^{248}$Cm, in panel (a); In panel (b), it shows distributions of reaction time to the angular momentum of collisions for these five reaction systems at incident energy $E_{\rm c.m.} = 1.1 \times V_{\rm B}$, which decreases exponentially with angular momentum increasing. For given angular momentum $L = 50\hbar$ in these five colliding systems, these internal excitation energies increase with reaction time exponentially in panel (c).

tendency of $V_{\rm CN}$ distributions for these collisions was similar. The larger Coulomb potential led to a larger interaction potential $V_{\rm CN}$. $V_{\rm CN}$ increase exponentially with distance R decreasing, in the attraction region of nuclear force where it increases slowly. Nucleon transfer happened at the touch configuration. Based on the deflection function, the sticking time of colliding partners was calculated for all impact parameters[49], shown in Fig. 2 (b), which decreases exponentially with angular momentum increasing. In these collisions, a relatively larger Coulomb potential cause a longer sticking time with the fixed impact parameter. During the sticking time, kinetic energy dissipates into the composite system to heat up with internal excitation energy, which increases with reaction time exponentially and reaches equilibrium around $2 \times 10^{-21}$ s, shown in Fig. 2 (c).

After capture for these colliding partners, the dissipating kinetic energy coupled to angular momentum in DNS enables them to diffuse along potential energy surface (PES), followed by nucleons rearrangement between the colliding partners, which was calculated by solving a set of master equations. PES and driving potential were calculated by Eq.(12) which were the composition of Coulomb potential, binding energy, and nuclear nuclear potential, computed by Wong formula, liquid-drop model plus shell correction, and double folding method[42], respectively. Driving potential of projectiles $^{208}$Hg, $^{208}$Pb and $^{208}$Po on targets $^{248}$Cm and $^{232}$Th at tip-tip collision with fixed distance plotted as a function of mass asymmetry $\eta$ respected to $\eta = (A_{\rm T} - A_{\rm P})/(A_{\rm T} + A_{\rm P})$, illustrated in Fig.3(a)(e), represented by solid black, dash red, dash-dot blue lines, respectively. Open circles and open stars stand for projectile-target injection points. From panels (a) and (e), it was found that the tendency of driving potential trajectories for these collisions was similar. There are two pockets that appear at $\eta = 0.2, 0$ for deriving the potential of target $^{248}$Cm-based reactions. One pocket in driving potentials for target $^{232}$Th-based reactions appears at $\eta = 0.2$.

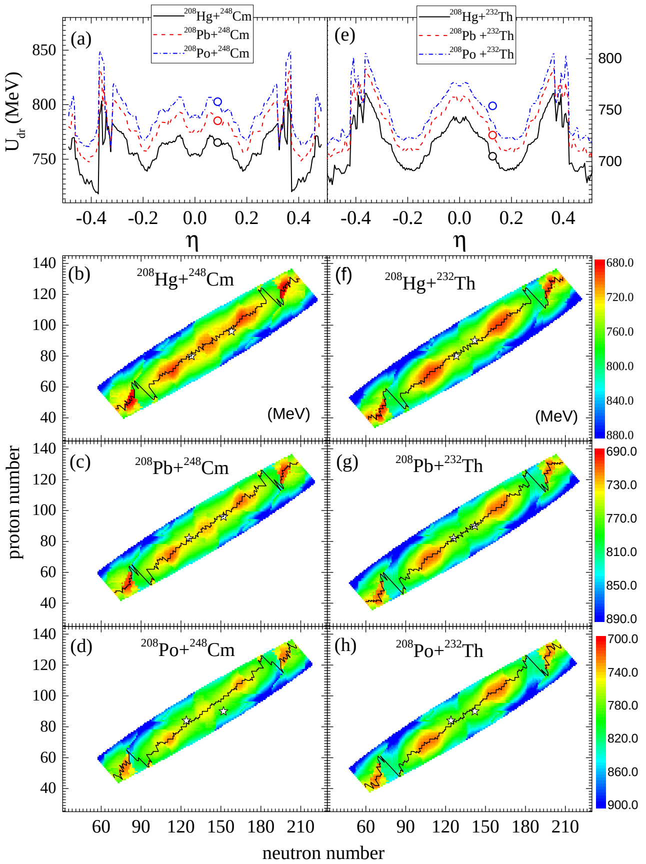


Fig. 3. (Color online) Potential energy surface and driver potentials of projectiles $^{208}$Hg, $^{208}$Pb and $^{208}$Po induced reactions with targets $^{248}$Cm and $^{232}$Th at tip-tip collisions were listed in Fig. 3. $^{208}$Hg, $^{208}$Pb and $^{208}$Po induced reactions were represented by solid black, dash red, and dash-dot blue lines in panels (a) and (e), respectively. Potential energy surfaces for these collisions were shown in panels (b), (c), (d), (f), (g), (h), respectively. Open stars stand for projectile-target injection points. These solid black lines were valley trajectories in two-dimensions potential energy surface.

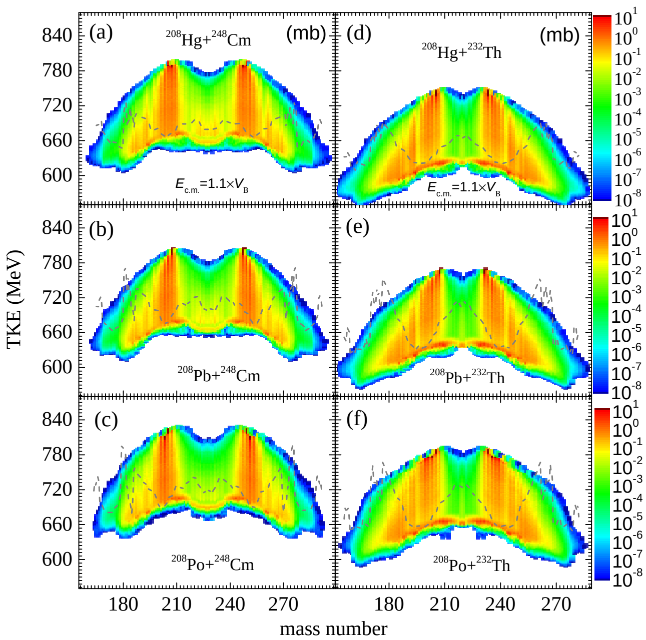


Fig. 4. (Color online) Calculated TKE-mass distribution of primary reaction products in head-on collisions of projectiles $^{208}$Hg, $^{208}$Pb and $^{208}$Po induced reactions with targets $^{248}$Cm and $^{232}$Th at $E_{\mathrm{c.m.}} = 1.1 \times V_{\mathrm{B}}$ were shown in panels (a), (b), (c), (d), (e) and (f), respectively, where driving potential trajectories were added in.

Neutron subshell number $N = 162$ might play a crucial role in pocket formation. For the projectiles $^{208}$Po far from $\beta-$ stable line, their injection points were far off their driving potential trajectories. When diffusion begins, it tends to the driving potential trajectory rapidly. In general, based on PES, the spectra distribution trend of each isotope chain has been predicted roughly.

Production probabilities of primary fragments with excitation energies were derived by solving a set of master equations, which were classified by mass number and kinetic energy, derived by Eq. (16), illustrated in Fig. 4, where driving potential trajectories were added as solid grey lines. From Fig. 4, it was found that two peaks in large kinetic regions located around projectile-target injection points and cross-sections prefer to populate around pockets of driving potential trajectories. For all the reactions of projectiles $^{208}$Hg, $^{208}$Pb and $^{208}$Po induced with targets $^{248}$Cm and $^{232}$Th at the incident energy $E_{\mathrm{c.m.}} = 1.1 \times V_{\mathrm{B}}$ gave the similar shape of TKE-mass distributions which have symmetric and broad distributions. The TKE-mass distribution is very wide in the kinetic range of 500 to 800 MeV and the mass region of 160 to 280, which might be expected to transfer more than 30 nucleons.

Based on the statistics evaporation program, the survival probability of excited primary fragments has been calculated, given the production cross-sections of secondary fragments. Production cross-sections of primary and secondary fragments as functions of mass number and charge number in collisions of projectiles $^{208}$Hg, $^{208}$Pb and $^{208}$Po induced reactions with targets $^{248}$Cm at $E_{\mathrm{c.m.}} = 1.1 \times V_{\mathrm{B}}$ were listed in Fig. 5 (a), (b), (c), (d), (e) and (f), respectively. Solid blue and dash red lines indicate secondary fragments and primary fragments. Superheavy nuclei region were covered by rectangular shadows. It was found that primary fragments could cover very large charge regions, even access the superheavy region, and secondary fragments were depressed by de-excitation strongly. Because highly excited primary trans-target fragments with small fission barriers led to fission easily. Predicted cross-sections of superheavy nuclei with $Z = 104 - 116$ were over 10 picobarns, where neutron subshell $N = 162$ might play a crucial role in, especially in collision of $^{208}$Po + $^{248}$Cm.

Calculated secondary production cross-sections of actinide target-like fragments of Actinium, Thorium, Protactinium, Uranium, Neptunium, Plutonium, Americium, Curium, Berkelium, Californium, Einsteinium, Fermium, Mendelevium, Nobelium, Lawrencium isotopes in collisions of projectiles $^{208}$Pt, $^{208}$Hg, $^{208}$Pb, $^{208}$Po, $^{208}$Rn, $^{208}$Ra bombarding on targets $^{248}$Cm at $E_{\mathrm{c.m.}} = 1.1 \times V_{\mathrm{B}}$, correspond to

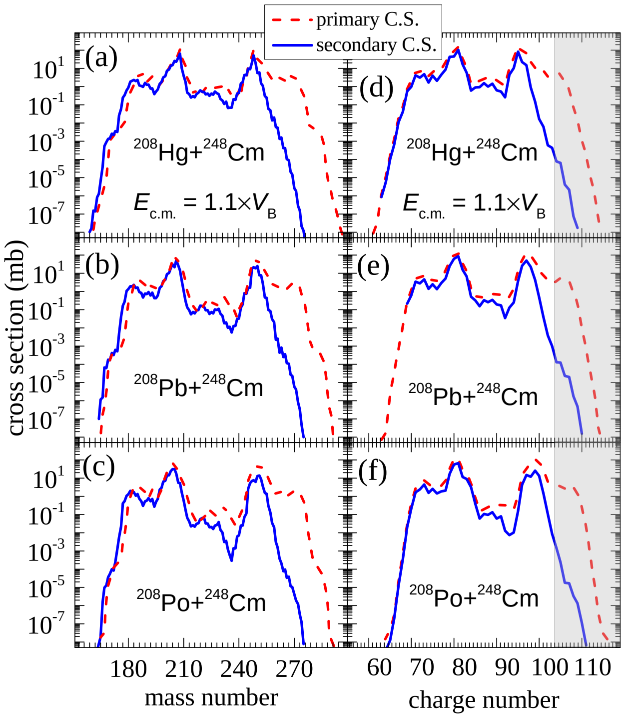


Fig. 5. (Color online) The calculated primary and secondary yields mass and charge distribution for $^{208}$Hg, $^{208}$Pb and $^{208}$Po induced reactions with targets $^{248}$Cm at $E_{\mathrm{c.m.}} = 1.1 \times V_{\mathrm{B}}$ were listed in panels (a), (b), (c), (d), (e) and (f), respectively. Dash red and solid blue lines represented primary and secondary yields. The superheavy region ($Z$ >104) were shown by rectangular shadow.

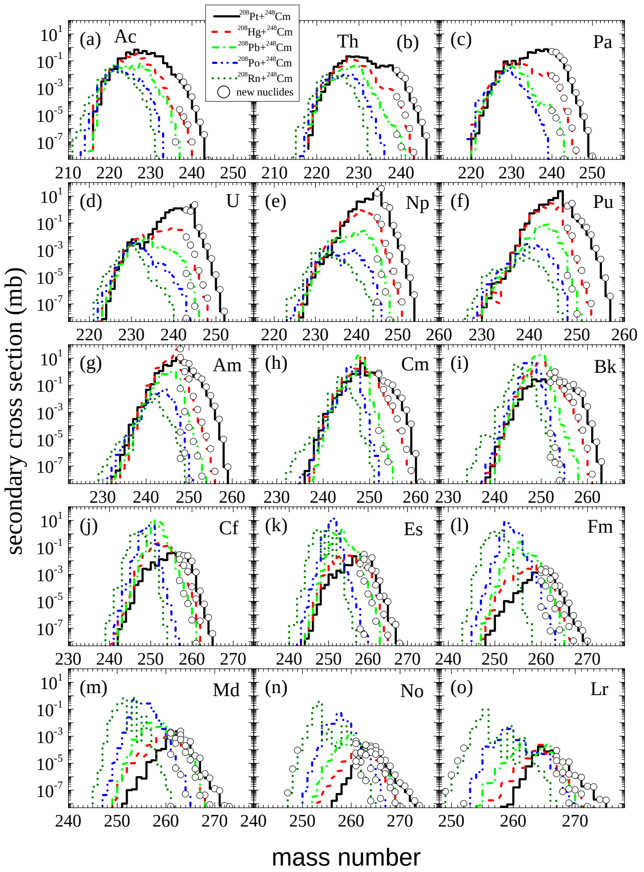


Fig. 6. (Color online) Predicted cross-sections of isotopic distribution of target-like fragments with $Z = 89 - 103$ in collisions of projectiles Pt, Hg, Pb, Po, Rn with mass number $A = 208$ bombarding on target $^{248}$Cm at $E_{\mathrm{c.m.}} = 1.1 \times V_{\mathrm{B}}$, correspond to solid black, dash red, dash-dot green, dash-dot-dot blue, and short dash olive lines, respectively, where predicted new actinide isotopes marked by open circles were added in.

solid black, dash red, dash-dot green, dash-dot-dot blue and short dash olive lines, respectively, illustrated in Fig. 6. It was found that collisions with the smaller Coulomb force prefer to shift to the neutron-rich region and with the larger Coulomb force tend to neutron-deficient area. Massive unknown actinide isotopes have been predicted by all of the reactions $^{208}$Pt+$^{248}$Cm, $^{208}$Hg+$^{248}$Cm, $^{208}$Pb+$^{248}$Cm, $^{208}$Po+$^{248}$Cm, $^{208}$Rn+$^{248}$Cm, $^{208}$Ra+$^{248}$Cm which is listed in Tab. 1. For new neutron-rich actinide isotopes, $^{208}$Pt+$^{248}$Cm reactions prefer to produce the largest cross-sections. However, $^{208}$Pt is still an unknown nucleus. It should be noticed that unknown actinide products are highly dependent on Coulomb potential. $^{208}$Rn+$^{248}$Cm reactions prefer to produce new neutron-deficient actinide isotopes with the largest cross-sections. The open circles represent new neutron-rich actinide nuclides.

Figure 7 shows secondary production cross-sections of all the formed fragments in collisions of $^{208}$Os+$^{248}$Cm, $^{208}$Pt+$^{248}$Cm, $^{208}$Hg+$^{248}$Cm, $^{208}$Pb+$^{248}$Cm, $^{208}$Po+$^{248}$Cm, $^{208}$Rn+$^{248}$Cm, $^{208}$Ra+$^{248}$Cm and primary production cross-sections of $^{208}$Pb+$^{248}$Cm at the incident energy $E_{\mathrm{c.m.}} = 1.1 \times V_{\mathrm{B}}$ as N-Z panel. Panels (g) and (h), clearly show the de-excitation effect. From panels (a), (b), (c), (d), (e), (f), and (h), it was found that massive new isotopes were predicted including neutron-rich and -deficient isotopes, even the superheavy nuclei. The projectile-target injection points and all the existing isotopes in the nuclide chart were represented by solid black-up triangles, and open squares, respectively.

## IV. CONCLUSION

Within the framework of DNS model, production cross-sections of MNT fragments in reactions of projectiles of $^{208}$Os, $^{208}$Pt, $^{208}$Hg, $^{208}$Pb,$^{208}$Po, $^{208}$Rn, $^{208}$Ra,$^{132,136}$Xe bombarding on targets of $^{232}$Th and $^{248}$Cm around Coulomb barrier energies have been calculated systematically. To investigate the isospin diffusion on the formation of actinide products in the MNT process, the same mass number of projectiles with $A = 208$ were selected. Our calculation of $^{132,136}$Xe + $^{248}$Cm have nicely consistent with the available experimental data. The sticking time of the colliding systems derived by deflection functions is highly dependent on the Coulomb force, especially at the small impact parameters. PES and TKE of these reactions are discussed, which could contribute to predicting the tendency of cross-section diffusion. The relatively large cross-section from TKE ap-

Table 1. The calculated cross sections of unknown actinide isotopes with Z=89-103 in the reactions of projectiles $^{208}$Pt, $^{208}$Hg and $^{208}$Pb induced MNT reactions with target $^{248}$Cm at incident energy $E_{\mathrm{c.m.}} = 1.1 \times V_B$.

| $^{248}$Cm + | $^{208}$Pt | $^{208}$Hg | $^{208}$Pb | $^{248}$Cm+ | $^{208}$Pt | $^{208}$Hg | $^{208}$Pb | $^{248}$Cm+ | $^{208}$Pt | $^{208}$Hg | $^{208}$Pb |
|---|---|---|---|---|---|---|---|---|---|---|---|
| $^{237}$Ac | 6.8 $\mu$b | 24 nb | | $^{254}$Pu | 1.3 $\mu$b | | | $^{261}$Es | 16 $\mu$b | 2.2 $\mu$b | 7.6 nb |
| $^{238}$Ac | 2.6 $\mu$b | 6.9 nb | | $^{255}$Pu | 0.2 $\mu$b | | | $^{262}$Es | 0.2 $\mu$b | 0.1 $\mu$b | 0.3 nb |
| $^{239}$Ac | 1 $\mu$b | 1.8 nb | | $^{256}$Pu | 8.4 nb | | | $^{263}$Es | 0.3 $\mu$b | 22 nb | 0.1 nb |
| $^{240}$Ac | 28 nb | 0.1 nb | | $^{248}$Am | 11 mb | 50 mb | 56 $\mu$b | $^{264}$Es | 23 nb | 1.1 nb | 30 pb |
| $^{241}$Ac | 2.8 nb | 0.5 pb | | $^{249}$Am | 4.5 mb | 1 mb | 1.1 $\mu$b | $^{265}$Es | 9.2 nb | 30 pb | |
| $^{239}$Th | 20 $\mu$b | 0.2 $\mu$b | 0.34 nb | $^{250}$Am | 3.9 mb | 0.3 mb | 74 nb | $^{260}$Fm | 1.3 $\mu$b | 2.1 $\mu$b | 0.3 $\mu$b |
| $^{240}$Th | 8.4 $\mu$b | 64.8 nb | 0.04 nb | $^{251}$Am | 1.1 mb | 14 $\mu$b | 6.6 nb | $^{261}$Fm | 2.4 $\mu$b | 1.4 $\mu$b | 0.1 $\mu$b |
| $^{241}$Th | 5 $\mu$b | 9.6 nb | | $^{252}$Am | 0.4 mb | 1.5 $\mu$b | | $^{262}$Fm | 1.6 $\mu$b | 0.4 $\mu$b | 16 nb |
| $^{242}$Th | 0.7 $\mu$b | 0.94 nb | | $^{253}$Am | 0.3 mb | 0.2 $\mu$b | | $^{263}$Fm | 0.7 $\mu$b | 0.1 $\mu$b | 2.8 nb |
| $^{243}$Th | 0.1 $\mu$b | 0.02 nb | | $^{254}$Am | 72 $\mu$b | 16 nb | | $^{264}$Fm | 0.1 $\mu$b | 5.8 nb | 0.08 nb |
| $^{244}$Th | 26 nb | | | $^{255}$Am | 17 $\mu$b | 1.9 nb | | $^{265}$Fm | 34 nb | 0.9 nb | |
| $^{245}$Th | 2.8 nb | | | $^{256}$Am | 2.7 $\mu$b | 40 pb | | $^{266}$Fm | 7 nb | 0.1 nb | |
| $^{246}$Th | 0.3 nb | | | $^{257}$Am | 0.3 $\mu$b | | | $^{267}$Fm | 0.9 nb | 10 pb | |
| $^{240}$Pa | 0.5 mb | 7.8 $\mu$b | 20. nb | $^{258}$Am | 9.7 nb | | | $^{261}$Md | 0.9 $\mu$b | 1.9 $\mu$b | 1.7 $\mu$b |
| $^{241}$Pa | 0.4 mb | 4.9 $\mu$b | 5.5 nb | $^{252}$Cm | 0.8 mb | 0.6 mb | 43 nb | $^{262}$Md | 0.6 $\mu$b | 0.6 $\mu$b | 0.2 $\mu$b |
| $^{242}$Pa | 0.2 mb | 1.1 $\mu$b | 0.5 nb | $^{253}$Cm | 0.2 mb | 47 $\mu$b | 1.9 nb | $^{263}$Md | 2.3 $\mu$b | 1.2 $\mu$b | 0.5 $\mu$b |
| $^{243}$Pa | 10 $\mu$b | 0.2 $\mu$b | 5 pb | $^{254}$Cm | 0.1 mb | 9.7 $\mu$b | 0.2 nb | $^{264}$Md | 0.5 $\mu$b | 0.2 $\mu$b | 62 nb |
| $^{244}$Pa | 28 $\mu$b | 17 nb | | $^{255}$Cm | 97 $\mu$b | 2.8 $\mu$b | 2 pb | $^{265}$Md | 0.4 $\mu$b | 74 nb | 18 nb |
| $^{245}$Pa | 3.3 $\mu$b | 1 nb | | $^{256}$Cm | 28 $\mu$b | 0.3 $\mu$b | | $^{266}$Md | 35 nb | 3.7 nb | 0.9 nb |
| $^{246}$Pa | 0.4 $\mu$b | 20 pb | | $^{257}$Cm | 11 $\mu$b | 40 nb | | $^{267}$Md | 23 nb | 1.1 nb | 40 pb |
| $^{247}$Pa | 74 nb | | | $^{258}$Cm | 1.4 $\mu$b | 1.7 nb | | $^{268}$Md | 1.6 nb | 40 pb | |
| $^{248}$Pa | 7.3 nb | | | $^{259}$Cm | 0.1 $\mu$b | 40 pb | | $^{269}$Md | 0.7 nb | 8 pb | |
| $^{249}$Pa | 0.6 nb | | | $^{260}$Cm | 0.8 nb | | | $^{261}$No | 6.3 nb | 54 nb | 47 nb |
| $^{250}$Pa | 9 pb | | | $^{252}$Bk | 0.2 mb | 0.7 mb | 36 $\mu$b | $^{262}$No | 12 nb | 64 nb | 219 nb |
| $^{243}$U | 0.9 mb | 9.1 $\mu$b | 18.4 nb | $^{253}$Bk | 0.3 mb | 0.9 mb | 1.9 $\mu$b | $^{263}$No | 0.1 nb | 206 nb | 68 nb |
| $^{244}$U | 0.7 mb | 2.2 $\mu$b | 2.2 nb | $^{254}$Bk | 0.2 mb | 0.1 mb | 0.1 $\mu$b | $^{264}$No | 0.2 nb | 131 nb | 47 nb |
| $^{245}$U | 2.2 mb | 0.5 $\mu$b | 70 pb | $^{255}$Bk | 0.1 mb | 46 $\mu$b | 14 nb | $^{265}$No | 0.1 nb | 86 nb | 5.4 nb |
| $^{246}$U | 46 $\mu$b | 29 nb | | $^{256}$Bk | 81 $\mu$b | 12 $\mu$b | 1.5 nb | $^{266}$No | 62 nb | 16 nb | 0.15 nb |
| $^{247}$U | 10 $\mu$b | 2.6 nb | | $^{257}$Bk | 0.1 mb | 5.2 $\mu$b | 0.3 nb | $^{267}$No | 16 nb | 2.6 nb | 0.01 nb |
| $^{248}$U | 1.7 $\mu$b | 0.3 nb | | $^{258}$Bk | 36 $\mu$b | 0.4 $\mu$b | 3 pb | $^{268}$No | 6 nb | 0.4 nb | |
| $^{249}$U | 0.2 $\mu$b | | | $^{259}$Bk | 22 $\mu$b | 46 nb | | $^{269}$No | 1.3 nb | 70 pb | |
| $^{250}$U | 14 nb | | | $^{260}$Bk | 2.5 $\mu$b | 2. nb | | $^{267}$Lr | 86 nb | 31 nb | 15 nb |
| $^{251}$U | 1.1 nb | | | $^{261}$Bk | 0.1 $\mu$b | 20 pb | | $^{268}$Lr | 12 nb | 2.1 nb | 0.6 nb |
| $^{245}$Np | 3.3 $\mu$b | 1 nb | | $^{261}$Bk | 6.1 nb | | | $^{269}$Lr | 17 nb | 1.5 nb | 0.1 nb |
| $^{246}$Np | 4.3 $\mu$b | 20 pb | | $^{257}$Cf | 27 $\mu$b | 12 $\mu$b | 0.3 $\mu$b | $^{270}$Lr | 1.2 nb | 0.1 nb | 6 pb |
| $^{247}$Np | 74 nb | | | $^{258}$Cf | 24 $\mu$b | 4.5 $\mu$b | 36 nb | $^{271}$Lr | 0.9 nb | 80 pb | 1 pb |
| $^{248}$Np | 7.3 nb | | | $^{259}$Cf | 23 $\mu$b | 1.6 $\mu$b | 6.5 nb | | | | |
| $^{249}$Np | 0.7 nb | | | $^{260}$Cf | 9.2 $\mu$b | 0.1 $\mu$b | 0.4 nb | | | | |
| $^{248}$Pu | 17 mb | 41 $\mu$b | 12.8 nb | $^{261}$Cf | 1.4 $\mu$b | 15 nb | 7 pb | | | | |
| $^{249}$Pu | 2.7 mb | 11 $\mu$b | 1.3 nb | $^{262}$Cf | 6.1 nb | 0.3 nb | | | | | |
| $^{250}$Pu | 0.3 mb | 0.2 $\mu$b | 0.019 nb | $^{263}$Cf | 0.6 nb | | | | | | |
| $^{251}$Pu | 0.1 mb | 30 nb | | $^{258}$Es | 7.4 $\mu$b | 6.2 $\mu$b | 1.1 $\mu$b | | | | |
| $^{252}$Pu | 48 $\mu$b | 2.4 nb | | $^{259}$Es | 29 $\mu$b | 13 $\mu$b | 0.3 $\mu$b | | | | |
| $^{253}$Pu | 13 $\mu$b | 10 pb | | $^{260}$Es | 11 $\mu$b | 3 $\mu$b | 34 nb | | | | |

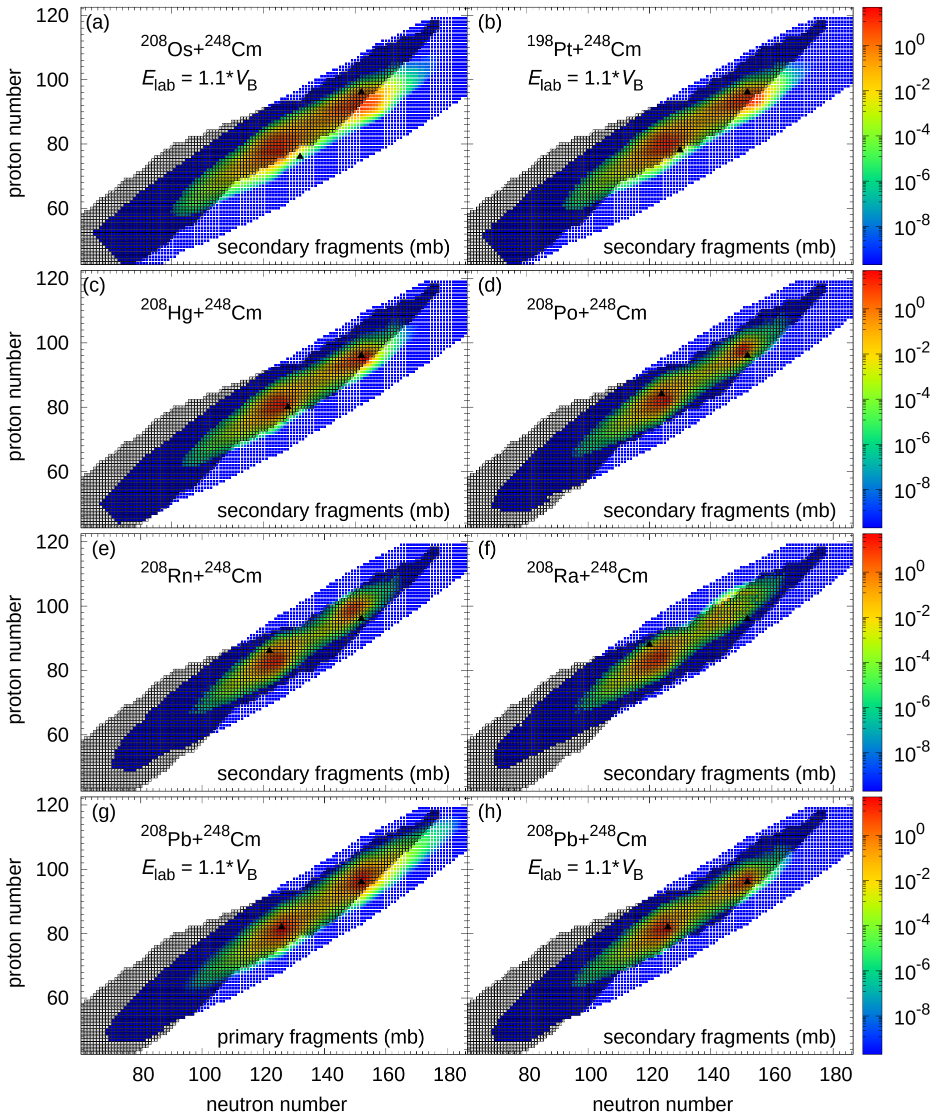


Fig. 7. (Color online) The production cross-section of secondary all the formed fragments in collisions of $^{208}$Pt + $^{248}$Cm, $^{208}$Hg + $^{248}$Cm, $^{208}$Pb + $^{248}$Cm, $^{208}$Po + $^{248}$Cm $^{208}$Rn + $^{248}$Cm and $^{208}$Ra + $^{248}$Cm at the incident energy $E_{\rm c.m.} = 1.1 \times V_{\rm B}$ and primary fragments of $^{208}$Pb + $^{248}$Cm were listed in $N - Z$ panels. Open stars stand for projectile-target injection points.



pears at around the pockets in PES, where the neutron subshell $N = 162$ exhibits evidently. The de-excitation process strongly depresses the primary cross-section of actinide isotopes up to four magnitude levels. The production cross-section of new actinides is highly dependent on the $N/Z$ ratio of the isobaric projectile. It is found that Coulomb force coupled with the shell effect plays a crucial role in the production cross-sections of actinides products in MNT reactions. Massive unknown heavy isotopes have been predicted with available cross-sections value by these five colliding systems, even for the superheavy nuclei with charge number $Z = 104-110$.

## V. ACKNOWLEDGEMENTS

This work was supported by National Natural Science Foundation of China (NSFC) (Grants No. 12105241,12175072), Natural Science Foundation of Jiangsu Province (Grants No. BK20210788), Jiangsu Provincial Double-Innovation Doctor Program(Grants No. JSSCBS20211013) and University Science Research Project of Jiangsu Province (Grants No. 21KJB140026) and Lv Yang Jin Feng of Yangzhou City (Grants No. YZ-LYJFJH2021YXBS130). This project was funded by the Key Laboratory of High Precision Nuclear Spectroscopy, Institute of Modern Physics, Chinese Academy of Sciences (CAS) (Grants No. IMPKFKT2021001).

## AUTHOR CONTRIBUTIONS

All authors contributed to the study conception and design. Material preparation, data collection and analysis were performed by Peng-Hui Chen, Chang Geng and Zu-Xing Yang. The first draft of the manuscript was written by Peng-Hui Chen and all authors commented on previous versions of the manuscript. All authors read and approved the final manuscript.


[1] K. Auranen, A.D. Briscoe, L.S. Ferreira, et al., Nanosecond-scale proton emission from strongly oblate-deformed $^{149}$Lu. Phys. Rev. Lett. **128**, 112501 (2022). doi:10.1103/PhysRevLett.128.112501

[2] H.B. Yang, Z.G. Gan, Z.Y. Zhang, et al., New isotope $^{207}$Th and odd-even staggering in $\alpha$-decay energies for nuclei with Z>82 and N<126. Phys. Rev. C **105**, L051302 (2022). doi:10.1103/PhysRevC.105.L051302

[3] T. Huang, D. Seweryniak, B.B. Back, et al., Discovery of the new isotope $^{251}$Lr: Impact of the hexacontetrapole deformation on single-proton orbital energies near the $z$ = 100 deformed shell gap. Phys. Rev. C **106**, L061301 (2022). doi:10.1103/PhysRevC.106.L061301

[4] Y.T. Oganessian, V.K. Utyonkov, N.D. Kovrizhnykh, et al., First experiment at the super heavy element factory: High cross section of $^{288}$Mc in the $^{243}$Am $+^{48}$ Ca reaction and identification of the new isotope $^{264}$Lr. Phys. Rev. C **106**, L031301 (2022). doi:10.1103/PhysRevC.106.L031301

[5] G.G. Kiss, A. Vitez-Sveiczer, Y. Saito, et al., Measuring the beta-decay properties of neutron-rich exotic pm, sm, eu, and gd isotopes to constrain the nucleosynthesis yields in the rare-earth region. The Astrophys. J. **936**, 107 (2022). doi:10.3847/1538-4357/ac80fc

[6] M. Huang, Z. Gan, Z. Zhang, et al., alpha decay of the new isotope $^{204}$Ac. Phys. Lett. B **834**, 137484 (2022). doi:https://doi.org/10.1016/j.physletb.2022.137484

[7] D.S. Ahn, J. Amano, H. Baba, et al., Discovery of $^{39}$Na. Phys. Rev. Lett. **129**, 212502 (2022). doi:10.1103/PhysRevLett.129.212502

[8] Y.T. Oganessian, V.K. Utyonkov, N.D. Kovrizhnykh, et al., New isotope $^{286}$Mc produced in the $^{243}$Am $+^{48}$ Ca reaction. Phys. Rev. C **106**, 064306 (2022). doi:10.1103/PhysRevC.106.064306

[9] M. Thoennessen, *The Discovery of Isotopes*, (Springer Nature, 2016)

[10] K.Y. Zhang, M.K. Cheoun, Y.B. Choi, et al., Nuclear mass table in deformed relativistic hartree–bogoliubov theory in continuum, I: Even–even nuclei. Atom. Data Nucl. Data **144**, 101488 (2022). doi:https://doi.org/10.1016/j.adt.2022.101488

[11] P. Möller, A.J. Sierk, T. Ichikawa, et al., Nuclear ground-state masses and deformations: FRDM(2012). Atom. Data Nucl. Data **109-110**, 1–204 (2016). doi:https://doi.org/10.1016/j.adt.2015.10.002

[12] P. Jachimowicz, M. Kowal, J. Skalski, Properties of heaviest nuclei with 98≤Z≤126 and 134≤N≤192. Atom. Data Nucl. Data **138**, 101393 (2021). doi:https://doi.org/10.1016/j.adt.2020.101393

[13] A. Såmark-Roth, D.M. Cox, D. Rudolph, et al., Spectroscopy along flerovium decay chains: Discovery of $^{280}$Ds and an excited state in $^{282}$Cn. Phys. Rev. Lett. **126**, 032503 (2021). doi:10.1103/PhysRevLett.126.032503

[14] Z.Y. Zhang, H.B. Yang, M.H. Huang, et al., New $\alpha$-emitting isotope $^{214}$U and abnormal enhancement of $\alpha$-particle clustering in lightest uranium isotopes. Phys. Rev. Lett. **126**, 152502 (2021). doi:10.1103/PhysRevLett.126.152502

[15] J. Khuyagbaatar, F.P. Heßberger, S. Hofmann, et al., $\alpha$ decay of $^{243}\mathrm{Fm}_{143}$ and $^{245}\mathrm{Fm}_{145}$, and of their daughter nuclei. Phys. Rev. C **102**, 044312 (2020). doi:10.1103/PhysRevC.102.044312

[16] N. Fukuda, T. Kubo, D. Kameda, et al., Identification of new neutron-rich isotopes in the rare-earth region produced by 345 MeV/nucleon $^{238}$U. J. Phys. Soci. J. **87**, 014202 (2018). doi:10.7566/JPSJ.87.014202

[17] H.M. Devaraja, S. Heinz, O. Beliuskina, et al., Observation of new neutron-deficient isotopes with Z ≥ 92 in multinucleon transfer reactions. Phys. Lett. B **748**, 199–203 (2015). doi:https://doi.org/10.1016/j.physletb.2015.07.006

[18] F.P. Hessberger, V. Ninov, D. Ackermann, et al., Production of heavy residues in nuclear collisions leading to $Z_p + Z_t \geq 75$ at bombarding energies of E/A = (11.4-15.3)MeV/u. Nucl. Phys. A **568**, 121–140 (1994). doi:https://doi.org/10.1016/0375-9474(94)90007-8

[19] A. Winther, Dissipation, polarization and fluctuation in grazing heavy-ion collisions and the boundary to the chaotic regime. Nucl. Phys. A **594**, 203–245 (1995). doi:https://doi.org/10.1016/0375-9474(95)00374-A

[20] A. Winther, Grazing reactions in collisions between heavy nuclei. Nucl. Phys. A **572**, 191–235 (1994). doi:https://doi.org/10.1016/0375-9474(94)90430-8

[21] Z.Q. Feng, G.M. Jin, J.Q. Li, Production of heavy isotopes in transfer reactions by collisions of $^{238}$U $+^{238}$ U. Phys. Rev. C **80**, 067601 (2009). doi:10.1103/PhysRevC.80.067601

[22] Z.Q. Feng, Production of neutron-rich isotopes around N = 126 in multinucleon transfer reactions. Phys. Rev. C **95**, 024615 (2017). doi:10.1103/PhysRevC.95.024615

[23] M. Huang, Z. Gan, X. Zhou, et al., Competing fusion and quasifission reaction mechanisms in the production of superheavy nuclei. Phys. Rev. C **82**, 044614 (2010). doi:10.1103/PhysRevC.82.044614

[24] L. Zhu, P.W. Wen, C.J. Lin, et al., Shell effects in a multinucleon transfer process. Phys. Rev. C **97**, 044614 (2018). doi:10.1103/PhysRevC.97.044614

[25] X.Q. Deng, S.G. Zhou, Examination of promising reactions with $^{241}$Am and $^{244}$Cm targets for the synthesis of new superheavy elements within the dinuclear system model with a dynamical potential energy surface. Phys. Rev. C **107**, 014616 (2023). doi:10.1103/PhysRevC.107.014616

[26] X.B. Yu, L. Zhu, Z.H. Wu, et al., Predictions for production of superheavy nuclei with Z = 105–112 in hot fusion reactions. Nucl. Sci. Tech. **29**, 154 (2018). doi:10.1007/s41365-018-0501-2

[27] P.H. Chen, F. Niu, Y.F. Guo, et al., Nuclear dynamics in multinucleon transfer reactions near coulomb barrier energies. Nucl. Sci. Tech. **29**, 185 (2018). doi:10.1007/s41365-018-0521-y

[28] F. Niu, P.H. Chen, H.G. Cheng, et al., Multinucleon transfer dynamics in nearly symmetric nuclear reactions. Nucl. Sci. Tech. **31**, 59 (2020). doi:10.1007/s41365-020-00770-1

[29] F. Niu, P.H. Chen, Z.Q. Feng, Systematics on production of superheavy nuclei Z = 119-122 in fusion-evaporation reactions. Nucl. Sci. Tech. **32**, 103 (2021). doi:10.1007/s41365-021-00946-3

[30] P.H. Chen, H. Wu, Z.X. Yang, et al., Prediction of synthesis cross sections of new moscovium isotopes in fusion-evaporation reactions. Nucl. Sci. Tech. **34**, 7 (2023). doi:10.1007/s41365-022-01157-0

[31] V. Zagrebaev, W. Greiner, Cross sections for the production of superheavy nuclei. Nucl. Phys. A **944**, 257–307 (2015). Special Issue on Superheavy Elements. doi:https://doi.org/10.1016/j.nuclphysa.2015.02.010

[32] D. Boilley, B. Cauchois, H. Lü, et al., How accurately can we predict synthesis cross sections of superheavy elements? Nucl. Sci. Tech. . doi:https://doi.org/10.1007/s41365-018-0509-7

[33] C. Golabek, C. Simenel, Collision dynamics of two $^{238}$U atomic nuclei. Phys. Rev. Lett. **103**, 042701 (2009). doi:10.1103/PhysRevLett.103.042701

[34] C. Simenel, Particle-number fluctuations and correlations in transfer reactions obtained using the balian-vénéroni variational principle. Phys. Rev. Lett. **106**, 112502 (2011). doi:10.1103/PhysRevLett.106.112502

[35] X. Jiang, N. Wang, Production mechanism of neutron-rich nuclei around N = 126 in the multi-nucleon transfer reaction $^{132}$Sn + $^{208}$Pb. Chin. Phys. C **42**, 104105 (2018). doi:10.1088/1674-1137/42/10/104105

[36] J.L. Tian, X.Z. Wu, K. Zhao, et al., Properties of the composite systems formed in the reactions of $^{238}$U +$^{238}$U and $^{232}$Th +$^{250}$ Cf. Phys. Rev. C **77**, 064603 (2008). doi:10.1103/PhysRevC.77.064603

[37] K. Zhao, Z.X. Li, X.Z. Wu, et al., Production probability of superheavy fragments at various initial deformations and orientations in the $^{238}$U+$^{238}$U reaction. Phys. Rev. C **88**, 044605 (2013). doi:10.1103/PhysRevC.88.044605

[38] V.V. Volkov, Deep inelastic transfer reactions — the new type of reactions between complex nuclei. Phys. Rep. **44**, 93–157 (1978). doi:https://doi.org/10.1016/0370-1573(78)90200-4

[39] G.G. Adamian, N.V. Antonenko, W. Scheid, et al., Treatment of competition between complete fusion and quasifission in collisions of heavy nuclei. Nucl. Phys. A **627**, 361–378 (1997). doi:https://doi.org/10.1016/S0375-9474(97)00605-2

[40] G.G. Adamian, N.V. Antonenko, W. Scheid, et al., Fusion cross sections for superheavy nuclei in the dinuclear system concept. Nucl. Phys. A **633**, 409–420 (1998). doi:https://doi.org/10.1016/S0375-9474(98)00124-9

[41] Z.Q. Feng, G.M. Jin, J.Q. Li, et al., Formation of superheavy nuclei in cold fusion reactions. Phys. Rev. C **76**, 044606 (2007). doi:10.1103/PhysRevC.76.044606

[42] Z.Q. Feng, G.M. Jin, F. Fu, et al., Production cross sections of superheavy nuclei based on dinuclear system model. Nucl. Phys. A **771**, 50–67 (2006). doi:https://doi.org/10.1016/j.nuclphysa.2006.03.002

[43] P.H. Chen, F. Niu, W. Zuo, et al., Approaching the neutron-rich heavy and superheavy nuclei by multinucleon transfer reactions with radioactive isotopes. Phys. Rev. C **101**, 024610 (2020). doi:10.1103/PhysRevC.101.024610

[44] P.H. Chen, Z.Q. Feng, J.Q. Li, et al., A statistical approach to describe highly excited heavy and superheavy nuclei. Chin. Phys. C **40**, 091002 (2016). doi:10.1088/1674-1137/40/9/091002

[45] G.G. Adamian, N.V. Antonenko, W. Scheid, Characteristics of quasifission products within the dinuclear system model. Phys. Rev. C **68**, 034601 (2003). doi:10.1103/PhysRevC.68.034601

[46] P. Grangé, L. Jun-Qing, H.A. Weidenmüller, Induced nuclear fission viewed as a diffusion process: Transients. Phys. Rev. C **27**, 2063–2077 (1983). doi:10.1103/PhysRevC.27.2063

[47] P.H. Chen, Z.Q. Feng, F. Niu, et al., Production of proton-rich nuclei around Z = 84-90 in fusion-evaporation reactions. Eur. Phys. J. A **53**,. doi:10.1140/epja/i2017-12281-x

[48] W. Nörenberg, Quantum-statistical approach to gross properties of peripheral collisions between heavy nuclei. Z. Phys. A **274**, 241–250 (1975). doi:10.1007/BF01437736

[49] J.Q. Li, G. Wolschin, Distribution of the dissipated angular momentum in heavy-ion collisions. Phys. Rev. C **27**, 590–601 (1983). doi:10.1103/PhysRevC.27.590

[50] W.F. Li, N. Wang, J.F. Li, et al., Fusion probability in heavy-ion collisions by a dinuclear-system model. Eur. Phys. Lett. (EPL) **64**, 750–756 (2003). doi:10.1209/epl/i2003-00622-0

[51] G. Wolschin, W. Nörenberg, Analysis of relaxation phenomena in heavy-ion collisions. Z. Phys. A **284**, 209–216 (1978). doi:10.1140/epja/i2017-12281-x

[52] C.Y. Wong, Interaction barrier in charged-particle nuclear reactions. Phys. Rev. Lett. **31**, 766–769 (1973). doi:10.1103/PhysRevLett.31.766

[53] I.I. Gontchar, D.J. Hinde, M. Dasgupta, et al., Double folding nucleus-nucleus potential applied to heavy-ion fusion reactions. Phys. Rev. C **69**, 024610 (2004). doi:10.1103/PhysRevC.69.024610

[54] P. Möller, Nuclear ground-state masses and deformations. At. Data Nucl. Data Tables **59**, 185–381 (1995). doi:https://doi.org/10.1006/adnd.1995.1002

[55] P. Demetriou, S. Goriely, Microscopic nuclear level densities for practical applications. Nucl. Phys. A **695**, 95–108 (2001). doi:https://doi.org/10.1016/S0375-9474(01)01095-8

[56] S. Cohen, W.J. Swiatecki, The deformation energy of a charged drop: Part v: Results of electronic computer studies. Annals Phys. **22**, 406–437 (1963). doi:https://doi.org/10.1016/0003-4916(63)90385-3

[57] G.G. Adamian, N.V. Antonenko, S.P. Ivanova, et al., Analysis of survival probability of superheavy nuclei. Phys. Rev. C **62**, 064303 (2000). doi:10.1103/PhysRevC.62.064303

[58] J.D. Jackson, A schematic model for (p, xn) cross sections in heavy elements. Can. J. Phys. **34**, 767–779 (1956). arXiv:https://doi.org/10.1139/p56-087, doi:10.1139/p56-087

[59] R.B. Welch, K.J. Moody, K.E. Gregorich, et al., Dependence of actinide production on the mass number of the projectile: Xe +$^{248}$Cm. Phys. Rev. C **35**, 204–212 (1987). doi:10.1103/PhysRevC.35.204

[60] K.J. Moody, D. Lee, R.B. Welch, et al., Actinide production in reactions of heavy ions with $^{248}$Cm. Phys. Rev. C **33**, 1315–1324 (1986). doi:10.1103/PhysRevC.33.1315